Front. Chem. Sci. Eng. 2023, 17(4): 470–482
https://doi.org/10.1007/s11705-022-2231-6

RESEARCH ARTICLE

Simultaneous removal of total oxidizable carbon, phosphate and various metallic ions from H_2O_2 solution with amino-functionalized zirconia as adsorbents

Yitong Wang[1], **Yue Zhang**[1], **Li Wang** (✉)[1,2]

1 School of Chemical Engineering and Technology, Tianjin University, Tianjin 300072, China
2 Zhejiang Institute of Tianjin University, Ningbo 315201, China

Abstract Amino-functionalized zirconia was synthesized by the co-condensation method using zirconium butanol and 3-aminopropyltriethoxy silane for the simultaneous removal of various impurities from aqueous 30% H_2O_2 solution. The results of Fourier transform infrared (FTIR) and Zeta potential showed that the content of N in amino-functionalized zirconia increased with the added amount of 3-aminopropyltriethoxy silane. Accordingly, the removal efficiency of total oxidizable carbon, phosphate and metallic ions from the H_2O_2 solution increased. The adsorbent with an N content of 1.62% exhibited superior adsorption performance. The removal efficiency of 82.7% for total oxidizable carbon, 34.2% for phosphate, 87.1% for Fe^{3+}, 83.2% for Al^{3+}, 55.1% for Ca^{2+} and 66.6% for Mg^{2+}, with a total adsorption capacity of 119.6 $mg \cdot g^{-1}$, could be achieved. The studies conducted using simulated solutions showed that the adsorption process of phosphate on amino-functionalized zirconia is endothermic and spontaneous, and the behaviors could be well described by the pseudo-second-order model and Langmuir model with a maximum adsorption capacity of 186.7 $mg \cdot g^{-1}$. The characterizations of the spent adsorbents by Zeta potential, FTIR and X-ray photoelectron spectroscopy revealed that the adsorption mechanism of phosphate is predominantly electrostatic attraction by the protonated functional groups and complementary ligand exchange with zirconium hydroxyl groups.

Keywords adsorption, zirconia, total oxidizable carbon, phosphate, metallic ions, hydrogen peroxide

1 Introduction

H_2O_2 is globally recognized as one of the 100 most important chemicals owing to its multifunctional and environmentally friendly properties [1]. In the electronics industry, H_2O_2 is widely utilized as a semiconductor silicon wafer cleaner, oxidation agent and etching agent for printed circuit boards [2]. Since the impurities in H_2O_2 solution are detrimental to electronic performance and integrated circuits, high-purity hydrogen peroxide is demanded. Currently, the anthraquinone process is the mainstream production technique of H_2O_2, occupying 98% of the global market [3]. The process involves the reduction of anthraquinone derivatives in an organic mixed solvent over a Pd catalyst, oxidation of the corresponding hydroquinone formed, extraction of H_2O_2 from the organic phase with deionized water and regeneration of the working solution [4]. A number of steps and the use of various chemicals, together with the addition of stabilizers (commonly H_3PO_4) during the operation for safety reasons, lead to the presence of various impurities in H_2O_2 solution. The impurities mainly include organic contaminants (total oxidizable carbon, TOC), metallic ions and acid radical anions (mainly phosphate). Hence, a post-purification step is required to produce high-purity H_2O_2 solution.

As reviewed by Luan et al. [5], the purification methods of H_2O_2 solution involve distillation, crystallization, ion exchange, membrane process and adsorption. Distillation and crystallization are usually energy intensive, with the requirement for pre-purification process. Various resins (cation exchange resins for the removal of metallic ions, anion exchange resins for acid radical anions and macroporous adsorption resins for TOC) are widely utilized for the purification of H_2O_2 solution. However, the resins could induce a decrease in the stability of H_2O_2, posing a safety risk [6]. Abejon et al. [7–9] systematically studied the reverse osmosis process for a 35% hydrogen peroxide solution produced by the anthraquinone process using polyamide membrane.

Received June 1, 2022; accepted August 5, 2022

E-mail: wlytj@tju.edu.cn

The contents of Na and Al ions were observed to decrease from 20895 and 1067 $\mu g \cdot L^{-1}$ to 1565 and 87 $\mu g \cdot L^{-1}$, respectively. The effective working time of the membrane was limited to 72 h due to the strong oxidation of H_2O_2. Lin et al. [10] found that commercial lignite activated carbon could significantly reduce TOC in a 35% H_2O_2 solution from 140 $mg \cdot L^{-1}$ to less than 20 $mg \cdot L^{-1}$ with a 2% decomposition rate of H_2O_2. In comparison, adsorption stands out from these methods because of low energy consumption, safe operation and easy handling [11–13]. However, the choice of adsorbent is a great challenge due to the severe separation conditions as a result of easy decomposition, strong acidity and oxidizability of H_2O_2 solution, and a variety of impurities (TOC, phosphate and metallic ions).

Metal oxide (ferric oxide, alumina and zirconia, etc.) and silica (including SBA-15, MCM-41 and MCM-48) have been extensively investigated due to their great potential as adsorbents [14–17]. Among them, zirconia has high chemical stability in both acidic and alkaline media [18]. Shehzad et al. [19] reported a good affinity for adsorbing arsenic species by mesoporous zirconia, with adsorption capacities of 105.0 and 110.3 $mg \cdot g^{-1}$ for As(III) and As(V) from aqueous solution, respectively. Song et al. [20] compared the adsorption capacity of amorphous, monoclinic and tetragonal zirconia for phosphate from aqueous solution and found that the amorphous zirconia has the highest adsorption capacity (102.6 $mg \cdot g^{-1}$) because of the largest content of hydroxyl groups. Ma et al. [21] reported the adsorption of phenolic acids and flavonoids using zirconia.

Amino functionalization with 3-aminopropyltriethoxy silane (APTES) is a simplified approach to improve the adsorption performance of oxide materials [22,23]. Majedi et al. [24] found that APTES-grafted zirconia exhibits higher adsorption capacity of Pb^{2+} and Cd^{2+} (147.1 and 75.2 $mg \cdot g^{-1}$) from aqueous solutions due to the strong complexation of amino groups. Mahmood et al. [25] reported the good adsorption of APTES-ZrO_2 for Cr(VI) species (anions) from aqueous solutions, which was attributed to the protonation of amino groups. Liu et al. [26] studied the adsorption of bovine serum albumin (BSA, a protein) on APTES-ZrO_2 from aqueous solutions and concluded that improved adsorption capacity results from the interaction between amino and carboxyl groups of BSA. Wang et al. [27] reported that the significantly improved performance of APTES-modified zirconia aerogels in NO_2 adsorption is ascribed to the interaction of protonated amino groups with NO_2. To our knowledge, there are few reports in the literature on the co-adsorption of different impurities over amino-functionalized zirconia.

The aim of this work is to explore the possibility of simultaneous adsorption removal of TOC, phosphate and metallic ions from an aqueous 30% technical grade H_2O_2 solution using amino-functionalized zirconia, and reveal the relationship between the removal efficiency of various impurities and the grafted amount, with a focus on the adsorption behaviors and adsorption mechanism of phosphate. First, amino-functionalized zirconia was prepared using zirconium butanol ($Zr(OC_4H_9)_4$) as a zirconium source and APTES as a grafting agent via the co-condensation method. Then, the as-prepared adsorbents were characterized by X-ray diffraction (XRD), Fourier transform infrared (FTIR), Thermogravimetric analysis (TGA), scanning electron microscope (SEM) and X-ray photoelectron spectroscopy (XPS). Finally, the performance in the simultaneous adsorption removal of TOC, metallic ions and phosphate from a real H_2O_2 solution was evaluated, and adsorption isotherms, kinetics, thermodynamics and mechanisms were studied using the simulated solutions.

2 Experimental

2.1 Materials

$Zr(OC_4H_9)_4$ (80 wt %) was purchased from Shanghai Macklin Biochemical Technology Co., Ltd. Cetyltrimethylammonium bromide (CTAB, 98%) and APTES (98%) were purchased from Tianjin HEOWNS Biochemical Technology Co., Ltd. KOH (99.99%) and H_3PO_4 (> 85 wt %) were purchased from Shanghai Aladdin Biochemical Technology Co., Ltd. Technical grade H_2O_2 solution (30 wt %) was purchased from Beijing Innochem Technology Co., Ltd. All chemicals were used without further purification.

2.2 Preparation of adsorbents

Amino-functionalized zirconia was synthesized by the co-condensation method with slight modification [28]. Initially, 24 mmol KOH and 0.6 mmol CTAB were dissolved in 50 mL deionized water at 80 °C for 0.5 h. Then, 4 mmol $Zr(OC_4H_9)_4$ and a desired amount of APTES (2, 4, 8 mmol) were added sequentially and the mixture was stirred for 3 h at 80 °C. The formed precipitate was separated by hot filtration, washed with deionized water and ethanol in turn, and then dried at 110 °C. The obtained solid and 70 mL ethanol were well mixed, and the suspension was refluxed at 80 °C for 6 h to remove surfactant. Finally, the solid was recovered by filtration and dried at 110 °C. The as-obtained samples were labeled as Zr-N-X, where X (0.5, 1 and 2) represented the molar ratio of APTES to $Zr(OC_4H_9)_4$ in the synthesis solution. For comparison, unfunctionalized zirconia (labeled as ZrO_2-UN) was synthesized according to the same procedures and conditions, without the addition of APTES.

2.3 Characterizations of absorbents

Elemental analysis was performed using a Vario EL elemental analyzer (Elementar, Germany). FTIR spectra were recorded on a Vertex 70 infrared spectrometer (Bruker, Germany). XRD patterns were recorded using a D8-Focus diffractometer (Bruker, Germany). Nitrogen adsorption−desorption isotherms were measured on a 3Flex surface characterization analyzer (Micromeritics, USA). TGA was performed on a TQ500 thermal analyzer (HENVEN, China). The morphology was observed by an S-4800 field emission scanning electron microscope (Hitachi, Japan). XPS was performed on an ESCALAB 250Xi photoelectron spectrometer (Thermo Fisher, USA). Zeta potential of adsorbents was measured by a Litesizer 500 analyzer (Anton Paar, Austria).

2.4 Adsorption experiments

2.4.1 Adsorption experiments using real H_2O_2 solution

Adsorption experiments were conducted in a round bottom flask (50 mL in volume) with a magnetic stirrer. Prior to adsorption, the pH and concentration of the H_2O_2 solution were determined. The adsorbent (20 mg) was added to 20 mL H_2O_2 solution and the mixture was stirred at 30 °C for 1 h. After adsorption, the H_2O_2 solution was sampled through a 0.22 μm filter membrane and then the pH was determined. The concentration of H_2O_2 in the sample was titrated with $KMnO_4$ solution. The contents of metallic ions, phosphate and TOC were measured by using a 7900 inductively coupled plasma-mass spectrometry (ICP-MS, Agilent, USA), an ICS 5000+ ion chromatography (Thermo Fisher, USA) and an Aurora 1030W TOC Analyzer (OI Analytical, USA), respectively. Prior to analysis, H_2O_2 in the sample was decomposed sufficiently at 50 °C for 96 h. Next, an additional ion-exchange procedure was performed using a cation-exchange resin column (10 cm × 1 cm) to remove metallic ions from the sample used for the analysis of phosphate. Three individual adsorption experiments were performed for each adsorbent tested to ensure the reproducibility of the results.

2.4.2 Adsorption experiments using simulated phosphate solutions

The adsorption kinetics, isotherms and thermodynamic experiments were performed with simulated phosphate solutions. The procedure and conditions (temperature, amount of adsorbent and solution) were the same as those mentioned above. The simulated phosphate solution was prepared by diluting phosphoric acid with deionized water. The pH value of the solution was adjusted to 3 with 1 mol·L^{-1} NaOH or HCl solution. The conditions for adsorption kinetics experiments were 30 °C and 200 mg·L^{-1} in phosphate concentration. Adsorption isotherm experiments were conducted at 30 °C and concentration varying from 100 to 500 mg·L^{-1} for 1 h. The conditions for thermodynamic studies were 200 mg·L^{-1} and temperatures ranging from 25 to 40 °C.

The adsorption capacity and removal efficiency of any individual impurity were calculated by using Eqs. (1) and (2),

$$q_{e,i} = \frac{(C_{0,i} - C_{e,i})V}{m}, \tag{1}$$

$$\text{Removal efficiency of impurity } i = \frac{C_{0,i} - C_{e,i}}{C_{0,i}} \times 100\%, \tag{2}$$

where $C_{0,i}$ and $C_{e,i}$ are the initial and residual concentration of any individual impurity (i = TOC, phosphate, Al^{3+}, Fe^{3+}, Ca^{2+} or Mg^{2+}), respectively, the unit for TOC and phosphate is mg·L^{-1}, while that for metallic ions is μg·L^{-1}; V is the volume of solution, mL; and m is the mass of adsorbent, mg.

2.5 Fitting and calculation methods

2.5.1 Kinetics fitting

The adsorption kinetics of phosphate on adsorbents were fitted by pseudo-first-order model (PFOM, Eq. (3)) and pseudo-second-order model (PSOM, Eq. (4)), respectively,

$$q_t = q_e(1 - e^{-K_1 t}), \tag{3}$$

$$\frac{t}{q_t} = \frac{1}{K_2 q_e^2} + \frac{t}{q_e}, \tag{4}$$

where q_e is the equilibrium adsorption capacity; q_t is the adsorption capacity at time t, mg·g^{-1}; and K_1 and K_2 are the rate constants.

2.5.2 Adsorption isotherm fitting

The adsorption isotherms of phosphate on adsorbents were fitted by the Langmuir (Eq. (5)) and Freundlich (Eq. (6)) models, respectively,

$$q_e = \frac{K q_{max} C_e}{1 + K C_e}, \tag{5}$$

$$q_e = K_F C_e^{1/n}, \tag{6}$$

where K is the Langmuir model coefficient; K_F and n are the Freundlich model constants; and q_{max} is the maximum adsorption capacity, mg·g^{-1}.

2.5.3 Thermodynamic properties calculation

The variation in the Gibbs free energy change (ΔG), enthalpy change (ΔH) and entropy change (ΔS) for the

adsorption process of phosphate on ZrO_2-UN and Zr-N-2 were calculated using Eqs. (7) and (8):

$$\Delta G = \Delta H - T\Delta S, \tag{7}$$

$$\ln\frac{q_e}{C_e} = \frac{\Delta S}{R} - \frac{\Delta H}{RT}, \tag{8}$$

where T is temperature, K. As seen from Eq. (8), the relationship between natural logarithm of q_e/C_e and $1/T$ should be linear. Hence, ΔH and ΔS can be calculated from the slope and intercept of such a plot.

3 Results and discussion

3.1 Composition and structure of adsorbents

3.1.1 Elemental analysis and XRD characterization

As presented in Table 1, the mass fraction of nitrogen in Zr-N-Xs increases significantly with the added amount of APTES, from 0 for ZrO_2-UN to 1.62 wt % for Zr-N-2 (ratio of APTES to $Zr(OC_4H_9)_4$ = 2).

As depicted in Fig. 1, ZrO_2-UN and Zr-N-Xs exhibit two "steamed bread" peaks at 30.2° and 50.6°, which are in accordance with the description on amorphous zirconia by Song et al. [20]. Both the intensity and position of the peaks for Zr-N-Xs are close to those for ZrO_2-UN, implying the preservation of the amorphous structure after grafting. This is in agreement with the observation by Rana et al. [28] on APTES-functionalized zirconia.

3.1.2 FTIR measurement

As depicted in Fig. 2, all adsorbents present a band at 1345 cm^{-1}, attributed to the deformation vibration of zirconium hydroxyl groups [19,29]. Additionally, bands corresponding to the stretching vibration of O–H at approximately 3420 cm^{-1} and the bending vibration of the adsorbed water molecules at 1630 cm^{-1} are observed for all samples.

For amino-functionalized zirconia, two new bands are observed at 1550 and 950 cm^{-1}. The former is assigned to the stretching vibration of N–H of free NH_2 groups [25,30], and the latter to Si–O–Zr vibration [26,30]. The intensity of N–H band strengthens with increasing N amount. This demonstrates the successful grafting of APTES. Furthermore, an extremely weak band is observed at 2900–3000 cm^{-1}, which is attributed to $-CH_2$ stretching vibration, accompanied by a decrease in the intensity of Zr–OH band. This suggests organic chains containing amino groups to be grafted into Zr–OH via the covalent bonding.

Table 1 Physicochemical properties of Zr-N-2 and ZrO_2-UN

Sample	N/%[a)]	D/nm[b)]	S_{BET}/($m^2 \cdot g^{-1}$)[c)]	V/($cm^3 \cdot g^{-1}$)[d)]
ZrO_2-UN	0	1.36/68.5	327.0	0.243
Zr-N-0.5	1.085	–	–	–
Zr-N-1	1.365	–	–	–
Zr-N-2	1.620	1.18	163.6	0.116

a) Mass fraction of nitrogen determined by elemental analysis; b) pore size calculated by the DFT model; c) specific surface area estimated by the BET (Brunauer–Emmett–Teller) method; d) total pore volume obtained at P/P_0 = 0.99.

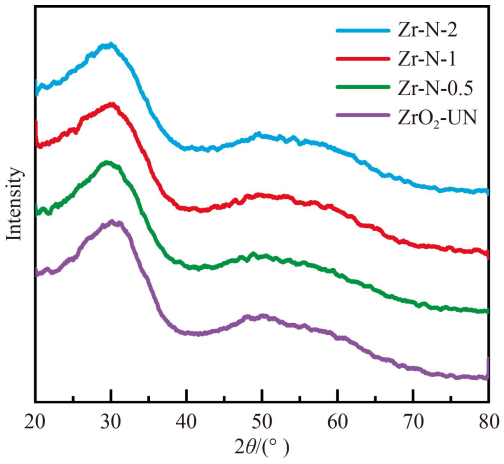

Fig. 1 XRD patterns of Zr-N-Xs and ZrO_2-UN.

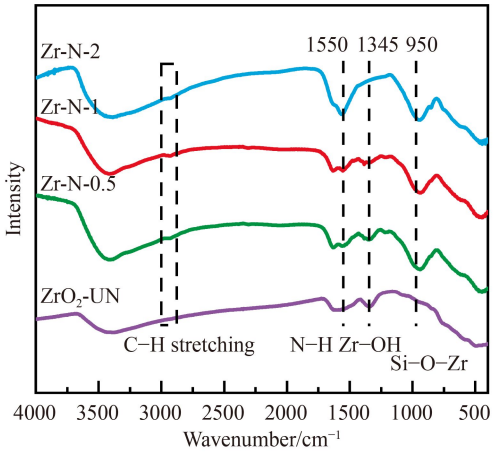

Fig. 2 FTIR spectra of Zr-N-Xs and ZrO_2-UN.

3.1.3 N_2 adsorption–desorption

The N_2 adsorption−desorption isotherms and pore size distributions of ZrO_2-UN and Zr-N-2 are displayed in Fig. S1 (cf. Electronic Supplementary Material, ESM). The two adsorbents present hybrid I–IV isotherms. ZrO_2-UN gives a broad size distribution with the pores centered at 1.36 and 68.5 nm. Zr-N-2 shows a decreased micropore size centered on 1.18 nm and obviously decreased amounts of meso- and macropores. This indicates that the grafting occurred preferentially inside the meso- and macropores. The textural properties calculated are listed in Table 1. The specific surface area and total pore volume of Zr-N-2 are apparently lower than those of

ZrO_2-UN, due to the embedding of organic chains into the pore interior blocking [31].

3.1.4 Thermogravimetric analysis

The TGA curves in Fig. 3 present two weight loss stages. The one at temperature below 100 °C is attributed to the dehydration of adsorbents, and the other at 100–500 °C is caused by the thermal decomposition of organic molecules. Moreover, the weight loss of Zr-N-Xs increases with the grafting amount and reaches a maximum value of 19.6% at the nitrogen content of 1.62% (Zr-N-2).

The peak temperature of ZrO_2-UN in the second stage of weight loss is 310 °C, lower than those of functionalized absorbents (340–350 °C). This could be explained by the difference in the decomposition temperature of organic molecules. The weight loss of ZrO_2-UN is caused by a residual surfactant inside the pore channels, and that of Zr-N-Xs is caused by the residual surfactant, as well as the grafted organic chains.

The shift in the peak temperature of Zr-N-Xs (from 350 °C for Zr-N-0.5 to 340 °C for Zr-N-2) could be attributed to the difference in the distribution of organic groups. An increase in the APTES dose would intensify the intermolecular competition, leading to some functional groups to be distributed on the outer surface of zirconia. The decomposition temperature of organic groups on the outer surface of materials is lower than that inside the pores [32]. As a result, the peak temperature shifts to a lower temperature.

3.1.5 Zeta potential

The Zeta potential measured for adsorbents at different pH values is provided in Fig. 4. Zr-N-Xs have the higher Zeta potential than ZrO_2-UN because amino groups are more susceptible to be protonated than hydroxyl groups [24]. The iso-electric point (IEP) of ZrO_2-UN is approximately 5.2. After amino-functionalization, the IEP monotonically shifts to high pH and Zr-N-2 has an IEP above 7. At pH of 3, all adsorbents show the highest Zeta potential, indicating the highest degree of protonation.

3.1.6 SEM analysis

Figure S2 (cf. ESM) shows the SEM images of adsorbents. It can be observed that ZrO_2-UN particles show agglomerated morphology for ordered microspheres with a uniform size. After functionalization, the morphology of Zr-N-2 significantly changes. The size of particles increases, and its distribution is no longer uniform. This could be ascribed to the nonuniform grafting of APTES, which is consistent with the observation on APTES-grafted zirconia by Mahmood et al. [25].

3.2 Adsorption of impurities from H_2O_2 solution

Figure 5 depicts the simultaneous adsorption results obtained for three types of impurities from the real H_2O_2 solution, including TOC, metallic ions and acid radical anions. The initial contents of these impurities are shown in Tables S1 and S2 (cf. ESM). The initial concentration and pH of the H_2O_2 solution were 29.38% and 2.79, respectively.

3.2.1 Removal efficiency of organic impurities

As depicted in Fig. 5(a), the removal efficiency of TOC on ZrO_2-UN is merely 1.7%. On functionalized zirconia, the removal efficiency of TOC is tremendously improved.

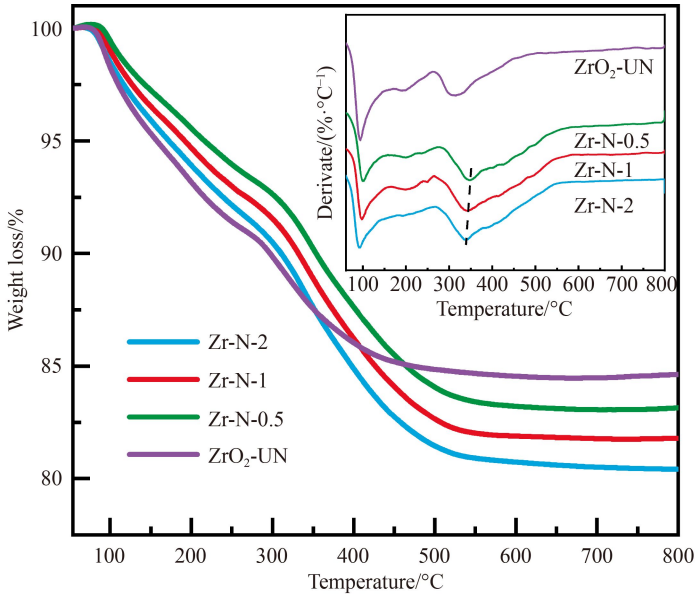

Fig. 3 TGA curves of Zr-N-Xs and ZrO_2-UN (inset: DTG curves).

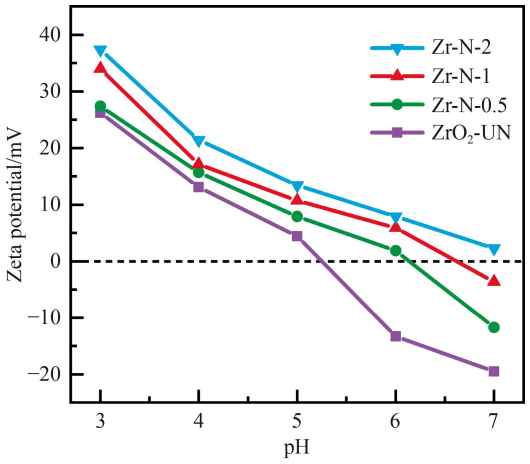

Fig. 4 Zeta potential of Zr-N-Xs and ZrO_2-UN.

This can be explained by the increased amino groups in Zr-N-Xs because of grafting. Organic impurities in H_2O_2 solution are mainly composed of alkyl-anthraquinone derivatives and C9–C10 heavy aromatic hydrocarbons. The amino groups could interact with benzene ring of alkyl-anthraquinones and heavy aromatic hydrocarbons through p-π conjugation, resulting in the improvement of adsorption affinity.

Generally, the decreased pore size of adsorbents limits the diffusion of organic molecules, which results in the amino groups inside the pore channels not being fully utilized. This is unfavorable for the adsorption of organic impurities. However, the removal efficiency of TOC increases monotonously with the nitrogen content, rendering a maximum value of 82.7% with the maximum adsorption capacity of 69.0 $mg \cdot g^{-1}$ (from 83.5 to 14.5 $mg \cdot L^{-1}$, as shown in Tables S2 and S3 (cf. ESM)) at the N content of 1.62% (Zr-N-2). This could be explained by the changed distribution of functional groups. With increasing the nitrogen content, the functional groups tend to be grafted on the outer surface of adsorbents, which could promote the adsorption of TOC because of the shortened diffusion length. The negative effect of decreasing pore size is canceled out by the effect of increasing amino groups on the outer surface. As a result, a positive effect of the grafting amount on the adsorption of TOC is obtained.

3.2.2 Removal efficiency of metallic ions

As seen in Table S1, there are a wide variety of metallic ions in the H_2O_2 solution, together with a broad distribution of contents ranging from 0 to 2705 $\mu g \cdot L^{-1}$. In this work, those metallic ions with contents above 60 $\mu g \cdot L^{-1}$ (Al^{3+}, Fe^{3+}, Ca^{2+}, Mg^{2+}, Na^{+} and K^{+}) were considered.

As presented in Fig. 5(b), amino-functionalized zirconia shows excellent adsorption affinity for Al^{3+} and Fe^{3+}. The removal efficiency of Al^{3+} and Fe^{3+} increases monotonously with the nitrogen content. Zr-N-2 gives the highest removal efficiency of Al^{3+} and Fe^{3+} with values of 83.2% and 87.1%, which increase by 16.5% and 36.4% compared with ZrO_2-UN. Accordingly, the contents of Fe^{3+} and Al^{3+} decrease to 9.7 from 75.2 $\mu g \cdot L^{-1}$ and 187.6 from 1115.8 $\mu g \cdot L^{-1}$, respectively (Tables S1 and S3). The removal efficiency of Mg^{2+} and Ca^{2+} exhibits a similar trend, and values of 66.6% and 55.1% are obtained for Mg^{2+} and Ca^{2+} on Zr-N-2, respectively. The total adsorption capacity of four metal ions is 1.8 $mg \cdot g^{-1}$. Both Zr-N-Xs and ZrO_2-UN have extremely weak adsorption for Na^{+} and K^{+} (not shown in Fig. 5(b)).

The difference in the adsorption capacity of ZrO_2-UN and Zr-N-Xs for metal ions results from different mechanisms. On ZrO_2-UN, metal ions ($M^{\alpha+}$) are adsorbed through ion exchange with unprotonated Zr–OH, forming Zr–O–M. On Zr-N-Xs, metal ions are adsorbed through ion exchange with Zr–OH and complexation with amino groups. The strong complexation ability between grafted amino groups and metal ions results in the enhancement of adsorption affinity. Since amino groups preferentially

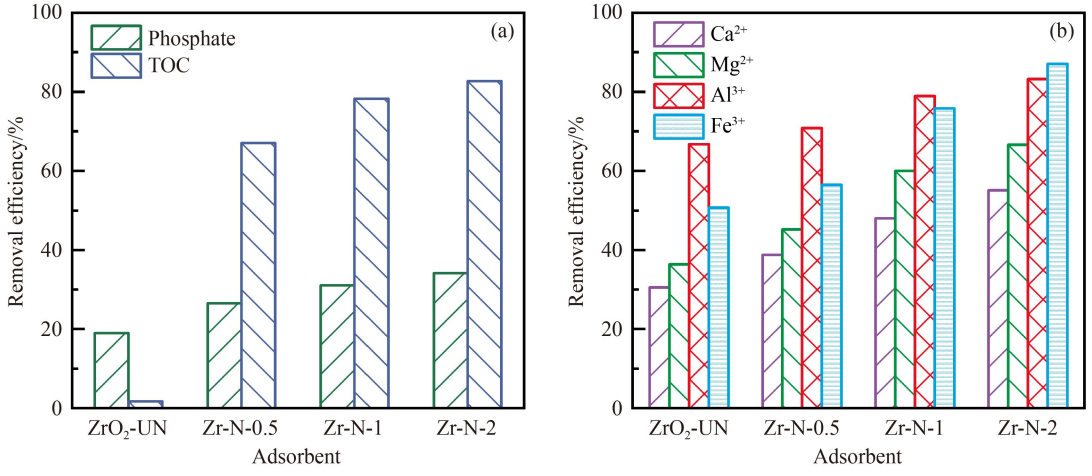

Fig. 5 Removal efficiency of (a) TOC and phosphate and (b) metallic ions from real H_2O_2 solution.

coordinate with highly charged metal ions having small radius [33], the high adsorption affinity for Fe^{3+} and Al^{3+} is obtained.

3.2.3 Removal efficiency of phosphate

As shown in Fig. 5(a), there is a monotonous increase in the removal efficiency with the nitrogen content, up to a maximum value of 34.2% at 1.62% (Zr-N-2), which represents a 1.8-fold increase compared to that on ZrO_2-UN (19.0%). Accordingly, the adsorption capacity of phosphate on Zr-N-2 is 48.8 $mg \cdot g^{-1}$ and the content in the adsorbed H_2O_2 solution decreases to 93.9 $mg \cdot g^{-1}$ (Table S3). Bacelo et al. [34] summarized that the adsorption mechanism of phosphate on metal oxides (La_2O_3 and CeO_2) involves electrostatic attraction and ligand exchange. Mahmood et al. [25] concluded that Cr(VI) anions are adsorbed by APTES-ZrO_2 through electrostatic attraction of protonated amino groups. Lam et al. [35] and Yokoi et al. [36] pointed out that the multivalent metallic ions adsorbed on aminopropyl-functionalized MCM-41 by complexation can serve as adsorption sites for anions, forming an alternating layer between positive cations and negative anions. In this work, however, the contribution of complexed metal ions to phosphate adsorption could be ignored because of much lower total adsorption capacity of metal ions (1.8 $mg \cdot g^{-1}$) than that of phosphate (48.8 $mg \cdot g^{-1}$). Therefore, the adsorption mechanism of phosphate might be electrostatic attraction and/or ligand exchange, which will be investigated and discussed in the following section of this work.

3.2.4 Effects of adsorbent on H_2O_2 decomposition

Since H_2O_2 is easy to be catalytically decomposed on the surface of some metal oxides, the concentration of H_2O_2 after adsorption was determined. As shown in Table 2, the decomposition rate of H_2O_2 on four adsorbents is relatively low, with a maximum value of 2.35% (from 29.38% before adsorption to 28.69% after adsorption). The main reason for the decomposition could be ascribed to the elevated pH of the H_2O_2 solution after adsorption (Table 2). The alkaline environment is unfavorable to the stabilization of hydrogen peroxide, expediting its decomposition to water [6].

Table 2 Adsorption results in the real H_2O_2 solution

Adsorbent	Concentration/%[a)]	pH[b)]	Zr^{4+}/($\mu g \cdot L^{-1}$)[c)]	q_e/($mg \cdot g^{-1}$)[d)]
ZrO_2-UN	29.18	3.60	3.1	29.7
Zr-N-0.5	29.10	4.12	7.1	95.1
Zr-N-1	28.89	4.78	12.3	111.3
Zr-N-2	28.69	5.10	18.7	119.6

a) Concentration of H_2O_2 solution after adsorption (initial concentration is 29.38%); b) pH of H_2O_2 solution after adsorption (initial pH is 2.79); c) content of Zr^{4+} in the H_2O_2 solution after adsorption (initial content is 1.9 $\mu g \cdot L^{-1}$); d) total adsorption capacity of TOC, Al^{3+}, Fe^{3+}, Ca^{2+}, Mg^{2+} and phosphate on adsorbents.

The leaching of Zr^{4+} in the adsorbed H_2O_2 solution was measured by ICP-MS and the results are summarized in Table 2. Zr-N-2 gives the maximum content, ranging from 1.9 $\mu g \cdot L^{-1}$ in the initial value to 18.7 $\mu g \cdot L^{-1}$, which is similar to the observation by Zhao et al. [11] for phosphate adsorption on a zirconium-based adsorbent (AL-DETA@Zr) from a simulated phosphate solution at pH of 3. The results prove the excellent stability of zirconium-based materials.

In summary, all three types of impurities from a real H_2O_2 solution could be adsorbed simultaneously on amino-functionalized zirconia. The grafting amount is shown to be a pivotal factor affecting the adsorption capacity of amino-functionalized zirconia. An increase in the amount of grafted amino groups could effectively enhance the affinity for adsorbing various impurities. However, the decomposition rate of H_2O_2 also increases with the grafted amount. Overall, Zr-N-2 having a nitrogen content of 1.62% is appropriate, with a total adsorption capacity of 119.6 $mg \cdot g^{-1}$ for TOC, four metallic ions (Al^{3+}, Fe^{3+}, Ca^{2+}, Mg^{2+}) and phosphate from the H_2O_2 solution (Table 2). Among three types of impurities, TOC shows the highest removal efficiency and adsorption capacity, although the content of phosphate is the highest. After adsorption, the content of TOC in the H_2O_2 solution decreased to 14.5 $mg \cdot L^{-1}$, lower than that (20 $mg \cdot L^{-1}$) reported by Lin [10]. This indicates that the simultaneous adsorption removal of multiple impurities using amino-functionalized zirconia as adsorbents may be a promising alternative for the purification of 30% technical grade H_2O_2 solution.

3.3 Adsorption of impurities from simulated solutions

As mentioned above, phosphate is the most abundant among all impurities in the H_2O_2 solution. Therefore, phosphate was chosen as an example to study the adsorption behaviors and mechanism using simulated phosphate solutions. The initial content and pH of the simulated phosphate solutions were determined according to typical values in the real H_2O_2 solution (Table S2).

3.3.1 Adsorption kinetics

Figure S3 (cf. ESM) depicts the effects of contact time on the removal of phosphate. At the initial period from 0 to 20 min, the adsorption capacity reaches approximately 90% of the corresponding equilibrium values. Then, the adsorption progressively approaches equilibrium within 60 min. This is attributed to the fast interaction between phosphate and active sites [37]. Therefore, an adsorption time of 1 h was chosen for the following experiments (adsorption isotherms and thermodynamics).

Figure 6 and Table S4 (cf. ESM) display the relevant results of the PFOM and PSOM. The PSOM shows

higher R^2 values compared to the PFOM for four adsorbents, indicating it to be more suitable for describing the adsorption of phosphate and the adsorption process to be dominated by chemisorption [38]. The results are in agreement with the other zirconium-based adsorbents, as summarized in Table S6 (cf. ESM).

3.3.2 Adsorption isotherms

The effects of initial concentration on the removal of phosphate are presented in Fig. S4 (cf. ESM). The adsorption capacity ascends rapidly with increasing phosphate concentration for all adsorbents. Compared with ZrO_2-UN, Zr-N-Xs have a higher adsorption capacity, ascribed to the contribution of grafted amino groups. As presented in Fig. 7 and Table S5 (cf. ESM), the Langmuir model shows larger R^2 values (> 0.94) than the Freundlich model, indicating the monolayer adsorption of phosphate on four adsorbents [39]. According to the fitting data of the Langmuir model, the maximum adsorption capacity (q_{max}) is obtained and the results are listed in Table S5. Zr-N-2 exhibits the highest q_{max} of 186.7 mg·g^{-1}, which outperforms most other zirconium-based adsorbents (Table S6).

We noted that the adsorption capacity of phosphate on Zr-N-2 is 91.7 mg·g^{-1} in the simulated solution with an initial concentration of 100 mg·L^{-1}, which is higher than that from the H_2O_2 solution (48.8 mg·g^{-1}), although the initial concentration of phosphate is close in these two cases. This implies the occurrence of interference in the case of the coexistence of various impurities. To test the hypothesis, a co-adsorption experiment was carried out on Zr-N-2 using a mixed solution containing 100 mg·L^{-1} phosphate and 100 mg·L^{-1} TMB (1,3,5-trimethylbenzene, a main component in C9–C10 heavy aromatic hydrocarbons) at the same pH, temperature and time. For the case of the coexistence of phosphate and TMB, the adsorption capacity of phosphate decreased to 73.7 mg·g^{-1}. That of TMB slightly dropped to 79.4 from 87.9 mg·g^{-1} (single TMB solution). This indicates that the adsorption of phosphate is hindered by coexisting TOC.

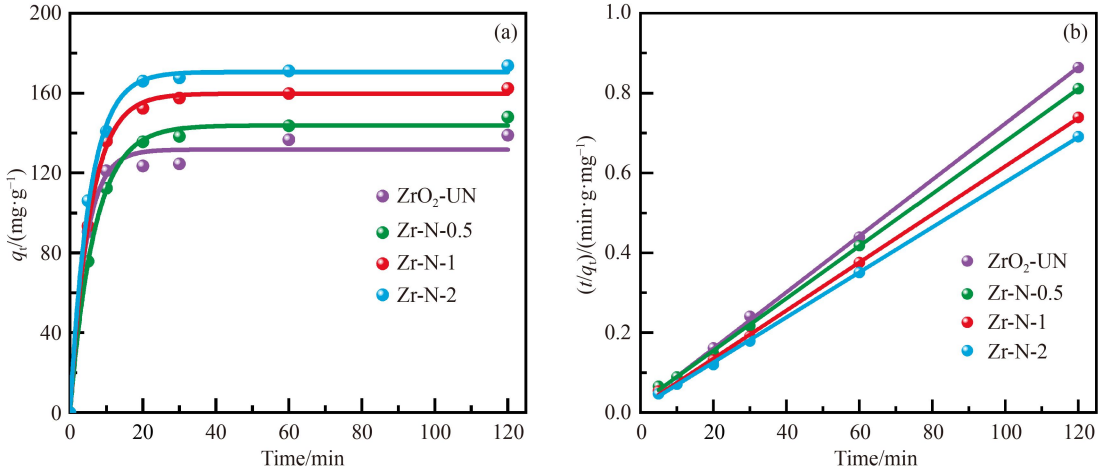

Fig. 6 Adsorption kinetics of phosphate at 30 °C and initial concentration of 200 mg·L^{-1}. (a) PFOM and (b) PSOM.

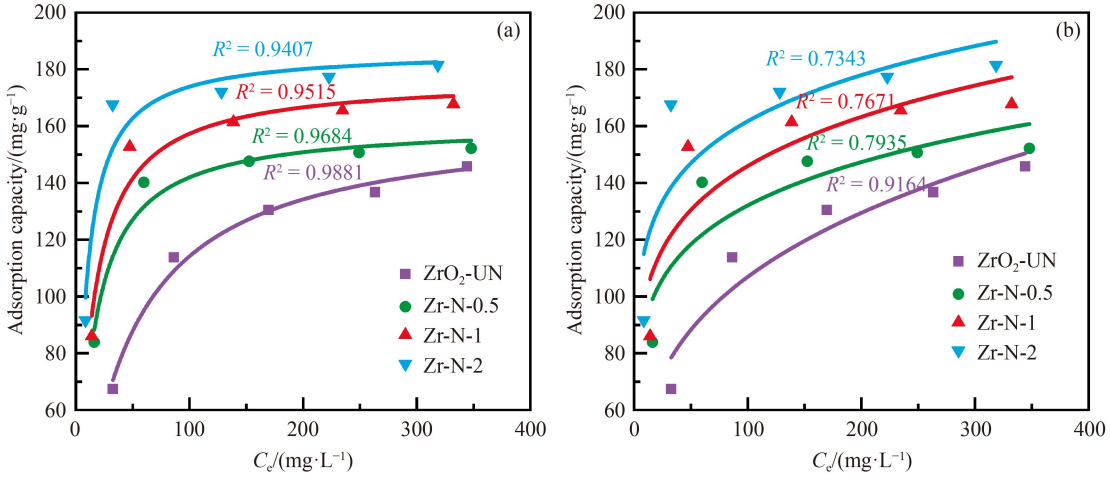

Fig. 7 Adsorption equilibrium isotherm of phosphate in simulated solution at pH 3 and 30 °C. (a) Langmuir model and (b) Freundlich model.

3.3.3 Adsorption thermodynamic studies

The effects of temperature on phosphate adsorption by Zr-N-2 and ZrO_2-UN are presented in Fig. S5 (cf. ESM). An increase in the adsorption capacity of phosphate with the temperature is revealed. In Fig. S6 (cf. ESM), a good linear relationship between $\ln(q_e/C_e)$ and $1/T$ is presented. The thermodynamic properties ΔH, ΔS and ΔG were calculated according to the slope and intercept of the plot, and the results are shown in Table 3. The positive values of ΔH indicate that the adsorption process of phosphate on ZrO_2-UN and Zr-N-2 is endothermic. The ΔG values remain negative from 25 to 40 °C, suggesting the spontaneity of phosphate adsorption. The positive ΔS values reflect an increase in the randomness during phosphate adsorption. A similar trend could be observed for phosphate uptake using zirconium-based adsorbent LBR-Zr [40].

3.4 Adsorption mechanism of phosphate

To further understand the adsorption mechanism of phosphate on amino-functionalized zirconia, the effects of initial pH on phosphate adsorption by ZrO_2-UN and Zr-N-2 were tested using simulated phosphate solutions with a concentration of 200 mg·L^{-1}. The spent adsorbents (used at pH of 3) were collected after adsorption and dried at 80 °C, named as S-ZrO_2-UN and S-Zr-N-2, and characterized by Zeta potential, FTIR and XPS.

3.4.1 Zeta potential of S-ZrO_2-UN and S-Zr-N-2

Figure 8 presents the Zeta potential of S-ZrO_2-UN and S-Zr-N-2. Compared with fresh adsorbents (Fig. 4), a decrease in the Zeta potential at pH of 3–7 is observed. The IEP of S-ZrO_2-UN is approximately 4.1, and that of S-Zr-N-2 is 4.6. A similar phenomenon was observed on amorphous zirconia reported by Su et al. [29]. This is due to the decrease in the amount of active Zr–OH and amino groups and the increased negative charge after phosphate adsorption.

3.4.2 FTIR of S-ZrO_2-UN and S-Zr-N-2

FTIR spectra of spent adsorbents are presented in Fig. 9. Compared with fresh ZrO_2-UN (Fig. 2), S-ZrO_2-UN appears to show a new broad band at 1044 cm^{-1} assigned to the vibration of P–O bond [41,42]. Moreover, the peak

Table 3 Thermodynamic properties for phosphate adsorption process on ZrO_2-UN and Zr-N-2

Sample	ΔG/(kJ·mol^{-1})				ΔH/ (kJ·mol^{-1})	ΔS/ (J·mol^{-1}·K^{-1})
	298.15 K	303.15 K	308.15 K	313.15 K		
ZrO_2-UN	–1.689	–1.940	–2.189	–2.376	12.10	46.28
Zr-N-2	–4.037	–4.482	–5.080	–5.510	25.90	100.36

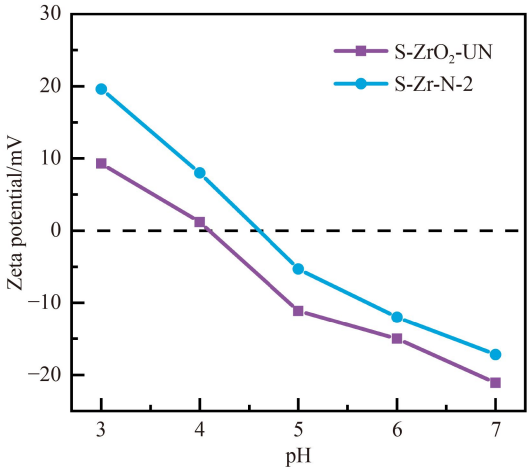

Fig. 8 Zeta potential of spent adsorbents (S-ZrO_2-UN and S-Zr-N-2 mean used ZrO_2-UN and Zr-N-2 in simulated phosphate solution of 200 mg·L^{-1} at pH = 3).

intensity of deformation vibration of Zr–OH at 1345 cm^{-1} is weakened after adsorption. This suggests that phosphate is adsorbed through ligand exchange between Zr–OH and phosphate [29], which is evidenced by the Zeta potential of S-ZrO_2-UN and S-Zr-N-2.

For S-Zr-N-2, the intensity of P–O bond is significantly stronger than that of S-ZrO_2-UN due to the higher adsorption capacity. However, the decrease in the intensity of Zr–OH peak is unobvious compared with that before adsorption (Zr-N-2), suggesting a low degree of ligand exchange between Zr–OH and phosphate. This implies the ligand exchange to be nondominant for phosphate adsorption on Zr-N-2. Moreover, the bending mode of amino groups at 1550 cm^{-1} weakens after adsorption and the band related to the protonated amino groups appears at 1510 cm^{-1} [43], indicating the existence of $-NH_3^+$ in S-Zr-N-2.

3.4.3 XPS of fresh and spent adsorbents

The XPS spectra of fresh (ZrO_2-UN and Zr-N-2) and spent (S-ZrO_2-UN and S-Zr-N-2) adsorbents are displayed in Fig. 10 and Fig. S7 (cf. ESM, survey spectra). In the O 1s spectra (Fig. 10(a)), the binding energies at 532.0, 531.3 and 530.1 eV are assigned to O in H_2O, Zr–OH and O^{2-} [29], respectively. The area ratio of Zr–OH decreased for both S-Zr-N-2 (from 46% to 39%) and ZrO_2-UN (from 49% to 28%). The results are in good agreement with those of FTIR in Fig. 9, where the decreased degree in the intensity of Zr–OH peak for S-Zr-N-2 is lower than that for S-ZrO_2-UN. This further demonstrates the minor portion of ligand exchange with Zr–OH in the adsorption of phosphate on Zr-N-2.

In the Zr 3d spectra (Fig. 10(b)), the binding energy of Zr 3d increased from 184.6 and 182.3 eV to 185.0 and 182.6 eV after phosphate adsorption. This is the result of

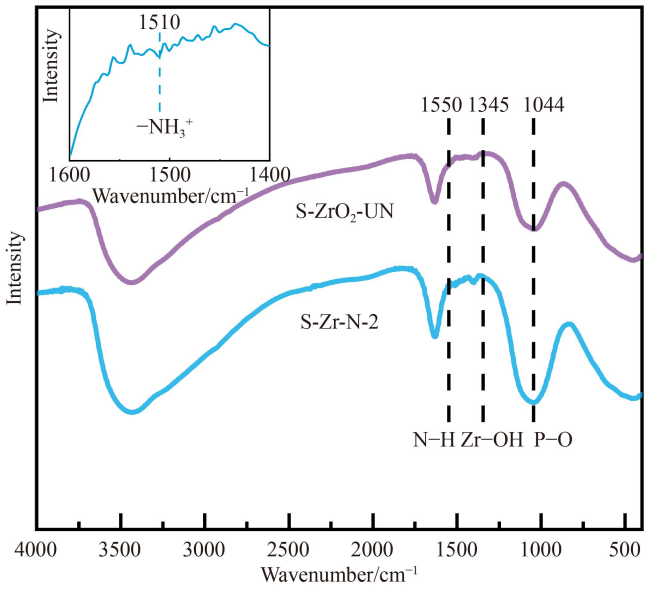

Fig. 9 FTIR spectra of spent adsorbents.

formation of Zr–O–P through the replacement of Zr–OH by phosphate. Since electronegativity of P (2.19) is higher than H (2.1) [40], the replacement results in the decrease of the electron density of Zr.

In the N 1s spectra of Zr-N-2 and S-Zr-N-2 (Fig. 10(c)), the binding energies of N 1s at 399.4 and 401.4 eV could be attributed to $-NH_2$ and $-NH_3^+$ [43]. For S-Zr-N-2, the binding energy of N related to $-NH_3^+$ species increased from 401.4 to 401.7 eV. This could be explained by the formation of P–O–NH_3^+ through electrostatic attraction with phosphate. As a result, the electron density of N minimizes because of the higher electronegativity of O than N. And much larger area ratio of $-NH_3^+$ than $-NH_2$ (77% vs. 23%) implies the dominant role of electrostatic attraction between $-NH_3^+$ and negatively charged phosphate in adsorption. We noted that Zr-N-2 has a relatively large area ratio of NH_3^+ species (54%). Yan et al. [43] concluded that NH_3^+ species could be formed on APTES-grafted SiO_2-AlOOH composite nanosheets by the interaction between grafted amino groups and surface hydroxyl groups.

As depicted in Fig. 10(d), the binding energy of P 2p for S-Zr-N-2 is lower than that for S-ZrO_2-UN, which implies a difference in P species. Shang et al. [44] reported that the P 2p spectra of adsorbed phosphate on quaternary-ammonium modified zirconia could be divided into two parts, and P species captured by ligand exchange show a slightly higher binding energy (0.7 eV) than those captured by electrostatic attraction. Hence, the P 2p peak of S-Zr-N-2 was deconvoluted. The peaks at 134.4 and 133.5 eV are assigned to Zr–O–P and P–O–NH_3^+, respectively. The area ratio of P–O–NH_3^+ is higher than that of Zr–O–P (59% vs. 41%). This suggests the dominant role of electrostatic attraction in phosphate adsorption.

3.4.4 Effects of initial pH

To further verify the adsorption mechanism of phosphate on amino-functionalized zirconia, the effects of initial pH on phosphate adsorption were investigated on Zr-N-2 and ZrO_2-UN, and the results are displayed in Fig. S8 (cf. ESM). The adsorption capacity of phosphate is greatly affected by initial pH. At pH of 3, the majority of NH_2 and a portion of Zr–OH are protonated, providing high electrostatic attraction for phosphate. The unprotonated Zr–OH could adsorb phosphate through ligand exchange between phosphate and Zr–OH. The electrostatic attraction combined with ligand exchange renders the highest adsorption capacity at pH of 3.

With increasing initial pH, the protonation degree of NH_2 and Zr–OH decreases. Therefore, the adsorption capacity gradually declines. At pH close to IEP (approximately 5.2 for ZrO_2-UN and above 7 for Zr-N-2), the adsorption capacity tends to be constant. It can be deduced that the adsorption of phosphate around IEP is dominated by ligand exchange between phosphate and Zr–OH.

For the case of adsorption dominated by ligand exchange, the adsorption capacity is affected by the density of Zr–OH. As shown in Fig. S8, although the density of Zr–OH in Zr-N-2 is lower than that of ZrO_2-UN because of grafting, the adsorption capacity around IEP on Zr-N-2 (pH of 7) is higher than that on ZrO_2-UN (pH of 5). This might be attributed to the formation of hydrogen bonding between $-NH_2$ and O of phosphate [23].

From the above analysis, it is reasonable to consider that the adsorption of phosphate on Zr-N-2 in the solution with pH of 3 is a multiplex process, which is dominated by the electrostatic attraction of protonated functional groups and complemented by the ligand exchange of

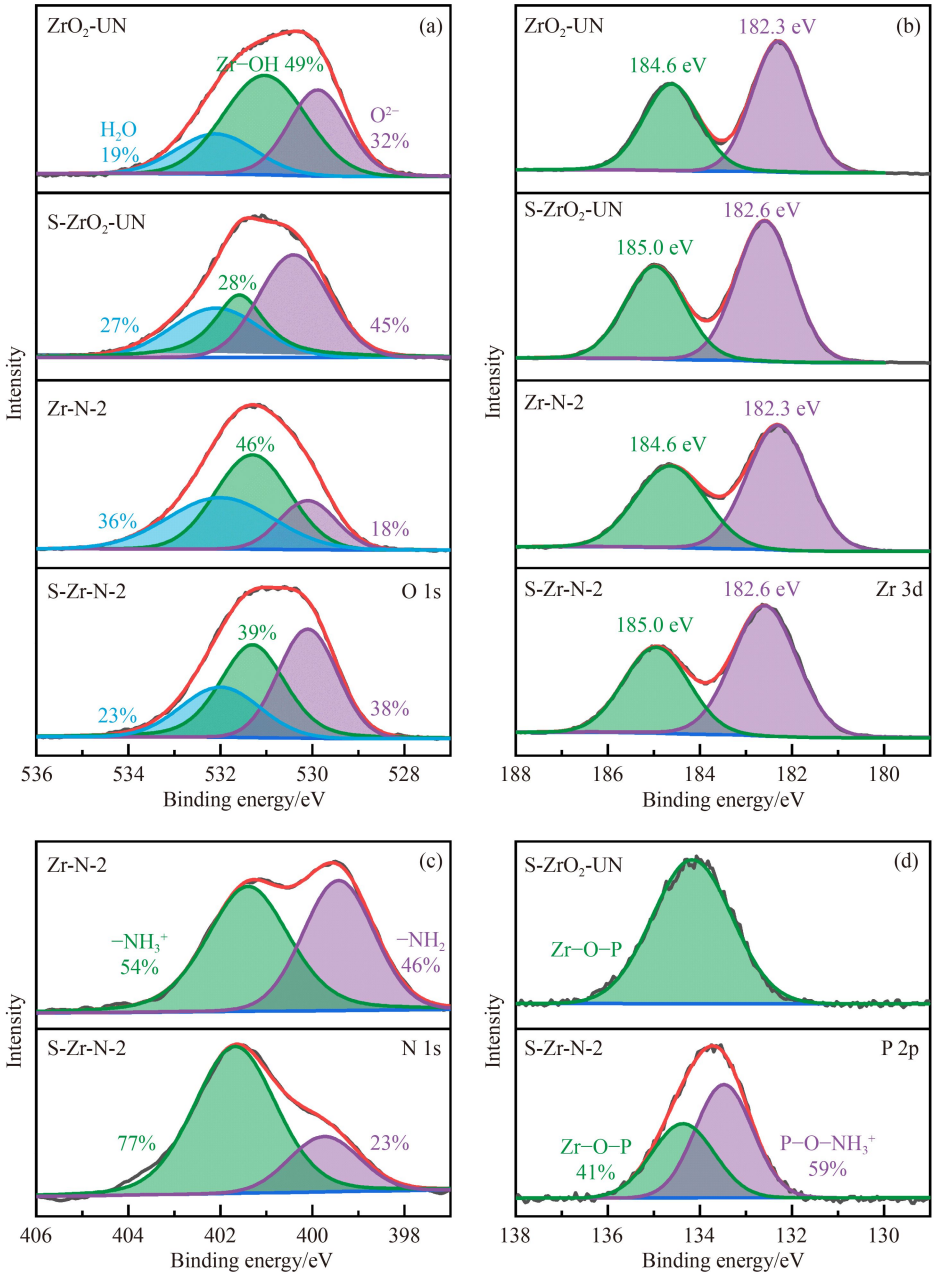

Fig. 10 XPS spectra of fresh and spent adsorbents. (a) O 1s spectra; (b) Zr 3d spectra; (c) N 1s spectra; (d) P 2p spectra.

hydroxyl groups, as shown in Scheme 1. Since the dominant species in the phosphate solution at pH = 2.12–7.21 is $H_2PO_4^-$, which gradually transforms to HPO_4^{2-} with increasing pH under acidic conditions [45], for brevity, only $H_2PO_4^-$ is shown as an example of phosphate in Scheme 1.

4 Conclusions

The simultaneous adsorption removal of multiple impurities from a real 30% technical grade H_2O_2 solution using amino-functionalized zirconia as adsorbents possesses feasibility. The grafted amount of amino groups had a positive effect on the removal efficiency of impurities. The functionalized zirconia with the N content of 1.62% had the highest removal efficiency of metallic ions (Fe^{3+}, Al^{3+}, Ca^{2+} and Mg^{2+}), TOC and phosphate from the H_2O_2 solution, with a total adsorption capacity of 119.6 $mg \cdot g^{-1}$ for metallic ions, TOC and phosphate. After adsorption, the content of TOC decreased to 14.5 $mg \cdot L^{-1}$.

The adsorption behaviors of phosphate on zirconia could be well fitted by the Langmuir adsorption isotherm and PSOM. The adsorption mechanisms of phosphate on amino-functionalized zirconia involve electrostatic attraction and ligand exchange. At pH of 3, the dominant mechanism is electrostatic attraction.

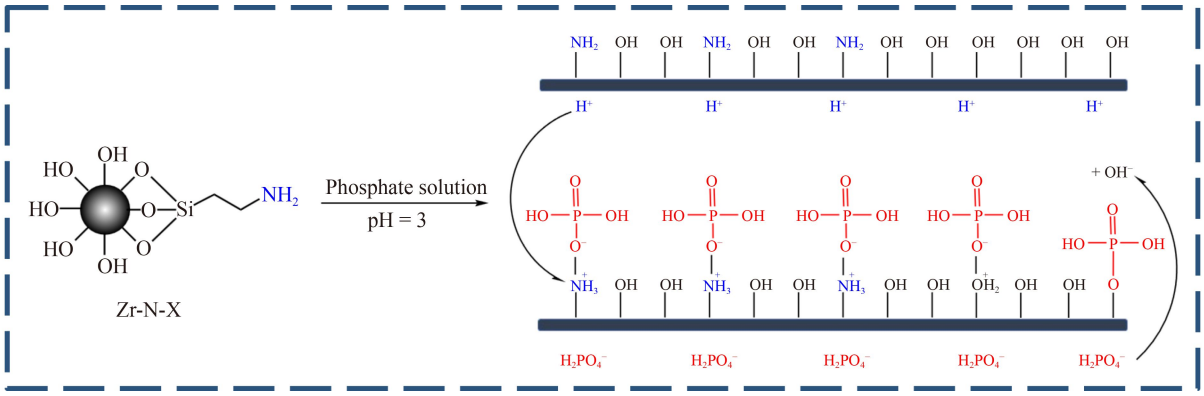

Scheme 1 Adsorption mechanisms of phosphate on amino-functionalized zirconia.

Acknowledgements This work was supported by the State Key Laboratory of Safety and Control for Chemicals (Grant No. 10010104-19-ZC0613-0180) and China Petrochemical Corporation Foundation (Grant No. 419005).

Electronic Supplementary Material Supplementary material is available in the online version of this article at https://dx.doi.org/10.1007/s11705-022-2231-6 and is accessible for authorized users.

References

1. Li H, Zheng B, Pan Z, Zong B, Qiao M. Advances in the slurry reactor technology of the anthraquinone process for H_2O_2 production. Frontiers of Chemical Science and Engineering, 2018, 12(1): 124–131
2. Bu Y, Wang Y, Han G, Zhao Y, Ge X, Li F, Zhang Z, Zhong Q, Baek J B. Carbon-based electrocatalysts for efficient hydrogen peroxide production. Advanced Materials, 2021, 33(49): 2103266
3. Liang J, Wang F, Li W, Zhang J, Guo C. Highly dispersed and stabilized Pd species on H_2 pre-treated Al_2O_3 for anthraquinone hydrogenation and H_2O_2 production. Molecular Catalysis, 2022, 524: 112264
4. Yuan E, Ren X, Wang L, Zhao W. A comparison of the catalytic hydrogenation of 2-amylanthraquinone and 2-ethylanthraquinone over a Pd/Al_2O_3 catalyst. Frontiers of Chemical Science and Engineering, 2017, 11(2): 177–184
5. Luan G, Gao W, Yao P. Progress on the preparation of ultra-pure hydrogen peroxide. Journal of Industrial and Engineering Chemistry, 2007, 13(7): 1047–1053
6. Zhang F, Chen M, Jia X, Xu W, Shi N. Research on the effect of resin on the thermal stability of hydrogen peroxide. Process Safety and Environmental Protection, 2019, 126: 1–6
7. Abejon R, Garea A, Irabien A. Integrated countercurrent reverse osmosis cascades for hydrogen peroxide ultrapurification. Computers & Chemical Engineering, 2012, 41: 67–76
8. Abejon R, Garea A, Irabien A. Ultrapurification of hydrogen peroxide solution from ionic metals impurities to semiconductor grade by reverse osmosis. Separation and Purification Technology, 2010, 76(1): 44–51
9. Abejon R, Garea A, Irabien A. Effective lifetime study of commercial reverse osmosis membranes for optimal hydrogen peroxide ultrapurification processes. Industrial & Engineering Chemistry Research, 2013, 52(48): 17270–17284
10. Lin Q, Jiang Y, Geng J, Qian Y. Removal of organic impurities with activated carbons for ultra-pure hydrogen peroxide preparation. Chemical Engineering Journal, 2008, 139(2): 264–271
11. Zhao Y, Shan X, An Q, Xiao Z, Zhai S. Interfacial integration of zirconium components with amino-modified lignin for selective and efficient phosphate capture. Chemical Engineering Journal, 2020, 398: 125561
12. Ouni L, Ramazani A, Fardood S T. An overview of carbon nanotubes role in heavy metals removal from wastewater. Frontiers of Chemical Science and Engineering, 2019, 13(2): 274–295
13. Wang L, Shi C, Wang L, Pan L, Zhang X, Zou J. Rational design, synthesis, adsorption principles and applications of metal oxide adsorbents: a review. Nanoscale, 2020, 12(8): 4790–4815
14. Xu P, Zeng G, Huang D, Feng C, Hu S, Zhao M, Lai C, Wei Z, Huang C, Xie G, Liu Z F. Use of iron oxide nanomaterials in wastewater treatment: a review. Science of the Total Environment, 2012, 424: 1–10
15. Hua M, Zhang S, Pan B, Zhang W, Lv L, Zhang Q. Heavy metal removal from water/wastewater by nanosized metal oxides: a review. Journal of Hazardous Materials, 2012, 211-212: 317–331
16. Cashin V B, Eldridge D S, Yu A, Zhao D. Surface functionalization and manipulation of mesoporous silica adsorbents for improved removal of pollutants: a review. Environmental Science. Water Research & Technology, 2018, 4(2): 110–128
17. Sonal S, Mishra B K. A comprehensive review on the synthesis and performance of different zirconium-based adsorbents for the removal of various water contaminants. Chemical Engineering Journal, 2021, 424: 130509
18. Lin J, Zhan Y, Wang H, Chu M, Wang C, He Y, Wang X. Effect of calcium ion on phosphate adsorption onto hydrous zirconium oxide. Chemical Engineering Journal, 2017, 309: 118–129
19. Shehzad K, Ahmad M, Xie C, Zhan D, Wang W, Li Z, Xu W, Liu J. Mesoporous zirconia nanostructures (MZN) for adsorption of As(III) and As(V) from aqueous solutions. Journal of Hazardous Materials, 2019, 373: 75–84
20. Song L, Li J, Zong H, Lin Y, Ding H, Huang L, Zhang P, Lai X,

Liu G, Fan Y. Zirconia nano-powders with controllable polymorphs synthesized by a wet chemical method and their phosphate adsorption characteristics & mechanism. Ceramics International, 2022, 48(5): 6591–6599

21. Ma Y, Zhu D, Wang C, Zhang Y, Shang Y, Liu F, Ye T, Chen X, Wei Z. Simultaneous and fast separation of three chlorogenic acids and two flavonoids from bamboo leaves extracts using zirconia. Food and Chemical Toxicology, 2018, 119: 375–379
22. Treccani L, Klein T Y, Meder F, Pardun K, Rezwan K. Functionalized ceramics for biomedical, biotechnological and environmental applications. Acta Biomaterialia, 2013, 9(7): 7115–7150
23. Wu B, Wan J, Zhang Y, Pan B, Lo I M C. Selective phosphate removal from water and wastewater using sorption: process fundamentals and removal mechanisms. Environmental Science & Technology, 2020, 54(1): 50–66
24. Majedi A, Davar F, Abbasi A. Citric acid-silane modified zirconia nanoparticles: preparation, characterization and adsorbent efficiency. Journal of Environmental Chemical Engineering, 2018, 6(1): 701–709
25. Mahmood T, Ullah A, Ali R, Naeem A, Farooq M, Aslam M. Amino functionalized zirconia as novel adsorbent for removal of Cr(VI) from aqueous solutions: kinetics, equilibrium, and thermodynamics studies. Desalination and Water Treatment, 2021, 210: 377–392
26. Liu G, Wu C, Zhang X, Liu Y, Meng H, Xu J, Han Y, Xu X, Xu Y. Surface functionalization of zirconium dioxide nano-adsorbents with 3-aminopropyl triethoxysilane and promoted adsorption activity for bovine serum albumin. Materials Chemistry and Physics, 2016, 176: 129–135
27. Wang X, Li K, Liang G, Zhao Y, Su R, Luan Z, Li L, Xi H. Amino-modified zirconia aerogels for the efficient filtration of NO_2: effects of water on the removal mechanisms. Environmental Science. Nano, 2021, 8(12): 3722–3734
28. Rana S, Mallick S, Parida K M. Facile method for synthesis of polyamine-functionalized mesoporous zirconia and its catalytic evaluation toward henry reaction. Industrial & Engineering Chemistry Research, 2011, 50(4): 2055–2064
29. Su Y, Cui H, Li Q, Gao S, Shang J. Strong adsorption of phosphate by amorphous zirconium oxide nanoparticles. Water Research, 2013, 47(14): 5018–5026
30. He Y, Jawad A, Li X, Atanga M, Rezaei F, Rownaghi A A. Direct aldol and nitroaldol condensation in an aminosilane-grafted Si/Zr/Ti composite hollow fiber as a heterogeneous catalyst and continuous-flow reactor. Journal of Catalysis, 2016, 341: 149–159
31. Ma Q, Wang N, Liu G, Wang L. Enhanced performance of Pd nanoparticles on SBA-15 grafted with alkyltrialkoxysilane in 2-ethyl-anthraquinone hydrogenation. Microporous and Mesoporous Materials, 2019, 279: 245–251
32. Wang L, Zhang Y, Ma Q, Pan Z, Zong B. Hydrogenation of alkyl-anthraquinone over hydrophobically functionalized Pd/SBA-15 catalysts. RSC Advances, 2019, 9(59): 34581–34588
33. Mongkol T, Phuwadej P, Anyarat W, Nagahiro S. Liquid-phase plasma-assisted in situ synthesis of amino-rich nanocarbon for transition metal ion adsorption. ACS Applied Nano Materials, 2020, 3(1): 218–228
34. Bacelo H, Pintor A M A, Santos S C R, Boaventura R A R, Botelho C M S. Performance and prospects of different adsorbents for phosphorus uptake and recovery from water. Chemical Engineering Journal, 2020, 381: 122566
35. Lam K F, Yeung K L, Mckay G. Selective mesoporous adsorbents for $Cr_2O_7^{2-}$ and Cu^{2+} separation. Microporous and Mesoporous Materials, 2007, 100(1-3): 191–201
36. Yokoi T, Tatsumi T, Yoshitake H. Fe^{3+} coordinated to amino-functionalized MCM-41: an adsorbent for the toxic oxyanions with high capacity, resistibility to inhibiting anions, and reusability after a simple treatment. Journal of Colloid and Interface Science, 2004, 274(2): 451–457
37. Liu B, Liu Z, Wu H, Pan S, Sun Y, Xu Y. Insight into simultaneous selective removal of nitrogen and phosphorus species by lanthanum-modified porous polymer: performance, mechanism and application. Chemical Engineering Journal, 2021, 415: 129026
38. Salehi E, Soroush F, Momeni M, Barati A, Khakpour A. Chitosan/polyethylene glycol impregnated activated carbons: synthesis, characterization and adsorption performance. Frontiers of Chemical Science and Engineering, 2017, 11(4): 575–585
39. Li F, Chen C, Wang Y, Li W, Zhou G, Zhang H, Zhang J, Wang J. Activated carbon-hybridized and amine-modified polyacrylonitrile nanofibers toward ultrahigh and recyclable metal ion and dye adsorption from wastewater. Frontiers of Chemical Science and Engineering, 2021, 15(4): 984–997
40. Zong E, Liu X, Jiang J, Fu S, Chu F. Preparation and characterization of zirconia-loaded lignocellulosic butanol residue as a biosorbent for phosphate removal from aqueous solution. Applied Surface Science, 2016, 387: 419–430
41. Wu B, Lo I M C. Surface functional group engineering of CeO_2 particles for enhanced phosphate adsorption. Environmental Science & Technology, 2020, 54(7): 4601–4608
42. Fu H, Yang Y, Zhu R, Liu J, Usman M, Chen Q, He H. Superior adsorption of phosphate by ferrihydrite-coated and lanthanum decorated magnetite. Journal of Colloid and Interface Science, 2018, 530: 704–713
43. Yan Z, Fu L, Yang H, Ouyang J. Amino-functionalized hierarchical porous SiO_2-AlOOH composite nanosheets with enhanced adsorption performance. Journal of Hazardous Materials, 2018, 344: 1090–1100
44. Shang Y, Xu X, Qi S, Zhao Y, Ren Z, Gao B. Preferable uptake of phosphate by hydrous zirconium oxide nanoparticles embedded in quaternary-ammonium Chinese reed. Journal of Colloid and Interface Science, 2017, 496: 118–129
45. Yang K, Yan L, Yang Y, Yu S, Shan R, Yu H, Zhu B, Du B. Adsorptive removal of phosphate by Mg−Al and Zn−Al layered double hydroxides: kinetics, isotherms and mechanisms. Separation and Purification Technology, 2014, 124: 36–42